Formation of HONO from the NH_3-promoted hydrolysis of NO_2 dimers in the atmosphere

Lei Li[a,b,c], Zhiyao Duan[b,c], Hui Li[d], Chongqin Zhu[a], Graeme Henkelman[b,c,1], Joseph S. Francisco[a,1], and Xiao Cheng Zeng[a,d,e,f,1]

[a]Department of Chemistry, University of Nebraska–Lincoln, Lincoln, NE 68588; [b]Department of Chemistry, The University of Texas at Austin, Austin, TX 78712; [c]Institute for Computational Engineering and Sciences, The University of Texas at Austin, Austin, TX 78712; [d]Beijing Advanced Innovation Center for Soft Matter Science and Engineering, Beijing University of Chemical Technology, Beijing 10029, China; [e]Department of Chemical and Biomolecular Engineering, University of Nebraska–Lincoln, Lincoln, NE 68588; and [f]Department of Mechanical and Materials Engineering, University of Nebraska–Lincoln, Lincoln, NE 68588

Contributed by Joseph S. Francisco, May 29, 2018 (sent for review May 4, 2018; reviewed by Bin Chen and Veronica Viada)

One challenging issue in atmospheric chemistry is identifying the source of nitrous acid (HONO), which is believed to be a primary source of atmospheric "detergent" OH radicals. Herein, we show a reaction route for the formation of HONO species from the NH_3-promoted hydrolysis of a NO_2 dimer ($ONONO_2$), which entails a low free-energy barrier of 0.5 kcal/mol at room temperature. Our systematic study of HONO formation based on NH_3 + $ONONO_2$ + nH_2O and water droplet systems with the metadynamics simulation method and a reaction pathway searching method reveals two distinct mechanisms: (*i*) In monohydrates (n = 1), tetrahydrates (n = 4), and water droplets, only one water molecule is directly involved in the reaction (denoted the single-water mechanism); and (*ii*) the splitting of two neighboring water molecules is seen in the dihydrates (n = 2) and trihydrates (n = 3) (denoted the dual-water mechanism). A comparison of the computed free-energy surface for NH_3-free and NH_3-containing systems indicates that gaseous NH_3 can markedly lower the free-energy barrier to HONO formation while stabilizing the product state, producing a more exergonic reaction, in contrast to the endergonic reaction for the NH_3-free system. More importantly, the water droplet reduces the free-energy barrier for HONO formation to 0.5 kcal/mol, which is negligible at room temperature. We show that the entropic contribution is important in the mechanism by which NH_3 promotes HONO formation. This study provides insight into the importance of fundamental HONO chemistry and its broader implication to aerosol and cloud processing chemistry at the air–water interface.

air–water interface | HONO | NO_2 dimer

Nitrous acid (HONO) is a major source of hydroxyl radicals (OHs), which are the primary oxidant in the troposphere (1, 2). OHs play a major role in initiating the removal of volatile organic compounds and hence determine the fate of many anthropogenic species in the atmosphere. The photolysis of HONO contributes up to 60% of the OH production in the daytime (2, 3). Seasonal observation of nitrate, ammonium, sulfate, and particulate matter (PM) of <2.5 μm (PM2.5) in North China is associated with a high concentration of HONO (4, 5). Recent studies have reported that HONO formation is responsible for the increase in secondary pollutants in Mexico City (6). Despite its importance, the source of HONO has not been fully understood. The predicted HONO concentration from currently known sources is much lower than that measured in different environments (7, 8). For example, the average HONO concentration in Beijing is ∼1.5 ppbv during the daytime, but the predicted HONO concentration is ∼50% lower (9). A recent HONO budget analysis in Western China suggests that an additional unknown HONO source is required to explain 60.8% of the observed HONO concentration in the daytime (10). The observed HONO concentration in Mexico City has also been reported ∼2 times higher than the predicted value (6). A lack of understanding of the HONO concentration suggests that one or more sources of HONO have yet to be identified.

Various chemical routes have been reported for HONO production, including direct emission from the combustion of fossil fuels or biomass (11, 12), gas-phase homogeneous reactions (13, 14), the reaction of NO_2 on heterogeneous surfaces (15, 16), and photolysis reactions of HNO_3 or NO_2 (17, 18). One major source of HONO is the surface hydrolysis of NO_2 through NO_2 dimerization, as proposed by Finlayson-Pitts et al. (19):

$$2NO_2 + H_2O \rightarrow HONO + HNO_3.$$

The surface hydrolysis of NO_2 was used to explain HONO formation at night. However, this reaction is rapidly deactivated on the surface of soot particles. Additionally, NO_2 hydrolysis on a heterogeneous surface is too slow (20–60 times) to be responsible for the unexpected high concentration of HONO observed in atmospheric measurements. The low reaction rate for NO_2 hydrolysis is largely due to its high activation energy. Chou et al. (20) reported that the direct formation of HONO from N_2O_4 hydrolysis requires overcoming an energy barrier as high as 30 kcal/mol. Chen and coworker (21) found that a barrier of ∼17.1 kcal/mol limits HONO formation via the $ONONO_2$ + $(H_2O)_2$ mechanism. Even on a water droplet, a moderate barrier of ∼7.4 kcal/mol (much higher than the value of k_BT at room temperature) is encountered.

Significance

As the primary source of "detergent" OH radicals, nitrous acid (HONO) plays an essential role in the chemistry of the atmosphere. Despite extensive studies, the source of HONO is still elusive. Although recent studies have shown the importance of reactive nitrogen compounds during aerosol formation, mechanistic insight into how these compounds react is still missing. Herein, based on Born–Oppenheimer molecular-dynamics simulations and free-energy sampling, we identified a formation mechanism for HONO via the NH_3-promoted hydrolysis of NO_2 dimer ($ONONO_2$) on water clusters/droplets. The near-spontaneous formation of HONO at the water–air interface sheds light on the catalytic role of water droplets in atmospheric chemistry. This finding provides not only a missing HONO source but also insight into HONO chemistry.

Author contributions: L.L., Z.D., H.L., C.Z., G.H., J.S.F., and X.C.Z. designed research; L.L., Z.D., and G.H. performed research; J.S.F. contributed new reagents/analytic tools; L.L., Z.D., H.L., C.Z., G.H., J.S.F., and X.C.Z. analyzed data; and L.L., Z.D., H.L., C.Z., G.H., J.S.F., and X.C.Z. wrote the paper.

Reviewers: B.C., Louisiana State University; and V.V., University of Colorado.

The authors declare no conflict of interest.

[1]To whom correspondence may be addressed. Email: henkelman@utexas.edu, francisc@purdue.edu, or xzeng1@unl.edu.

This article contains supporting information online at www.pnas.org/lookup/suppl/doi:10.1073/pnas.1807719115/-/DCSupplemental.

Published online June 25, 2018.

Studies have shown that atmospheric ammonia can catalyze atmospheric reactions and effectively promote the transformation of chemical species in the atmosphere. Tao and coworkers (22) have reported the promoting role of ammonia in the hydrolysis of SO_2. Recent studies have also provided theoretical evidence that ammonia can facilitate the decomposition of carbonic acid, the isomerization of methoxy radical, and the •OH + HCl reaction (23–25). More recently, ammonia at the interface of a cloud droplet has been shown to catalyze the barrierless formation of ammonium sulfate in the atmosphere (26). Ammonia is the only basic gaseous molecule in the atmosphere and has a concentration ranging from ∼30 ppb in a modestly polluted atmosphere to 10 ppm in heavily polluted areas (27, 28). Recent satellite measurements and integrated cross-scale modeling show that ammonia tends to accumulate on the surface of cloud droplets (29). Additionally, recent field measurements have shown a correlation between the concentration of HONO and that of NH_3 (30, 31). Zhang and coworkers (32) have shown that the efficient formation of sulfate (one of the main constituents of fine PM) from the aqueous oxidation of SO_2 by NO_2 is observed in the presence of NH_3 under cloud conditions, using a combination of atmospheric measurements and laboratory experiments. Tao and coworkers (33) have also found via ab initio calculations that gaseous NH_3 can potentially promote the formation of HONO species. Motivated by these studies, we systematically studied HONO formation from the hydrolysis of a NO_2 dimer ($ONONO_2$) with or without the presence of NH_3 at the air–water interface using several theoretical methods, including molecular dynamics, metadynamics, reaction pathway determination, and thermodynamic integration. Two different formation mechanisms for HONO were identified in our metadynamics simulations, which were confirmed by reaction pathway calculations. Last, thermodynamic integration was used to compute the free-energy profile for the NH_3-free and NH_3-containing hydrolysis reaction of $ONONO_2$ to clarify the role of NH_3 in promoting the formation of the HONO species.

Results and Discussion

Since first reported by Finlayson-Pitts et al. (19), the asymmetric isomer $ONONO_2$ has been considered as an intermediate in the hydrolysis of NO_2. Recent spectroscopic evidence reported by Stanton and coworkers (34) confirms the formation of asymmetric $ONONO_2$ from the dimerization of NO_2 in the gas phase. It has also been observed that symmetric N_2O_4 converts to asymmetric $ONONO_2$ with a very short lifetime, even on an ice surface at 130 K (35). Hence, among the nitrogen oxides in the atmosphere, $ONONO_2$ is selected as a starting point to study the hydrolysis of NO_2 in the presence of NH_3. For brevity, the $N_2O_4 + (H_2O)_n + NH_3$ systems considered here are denoted monohydrate, dihydrate, trihydrate, and tetrahydrate systems with n = 1–4, respectively.

First, we performed 100-ps Born–Oppenheimer molecular-dynamics (BOMD) simulations for the dihydrate, trihydrate, and tetrahydrate systems to obtain a set of stable structures. These structures (Fig. 1*A*) were then used for the initial state of metadynamics simulations to explore possible reaction paths. For the monohydrate, a hand-built structure was used. The height and width of the Gaussian functions used in the metadynamics simulations were 0.003 eV and 0.1 Å, respectively; a new Gaussian was added every 30 steps. These parameters aim to preserve accurate small barriers for the tetrahydrate system, while ensuring that the reaction occurs within 10 ps for the higher barrier reactions in the monohydrate system (*SI Appendix*, Fig. S1). The N–H distance ($d_{N\text{-}H}$, noted in Fig. 1*A*) is used as the collective variable. A quadratic wall is applied when $d_{N\text{-}H} > 2.5$ Å to narrow the sampling space. Note that all metadynamics simulations were stopped when a reaction was detected. Although convergence of the free-energy surface is not always guaranteed in metadynamics, our approximate free-energy surfaces allowed

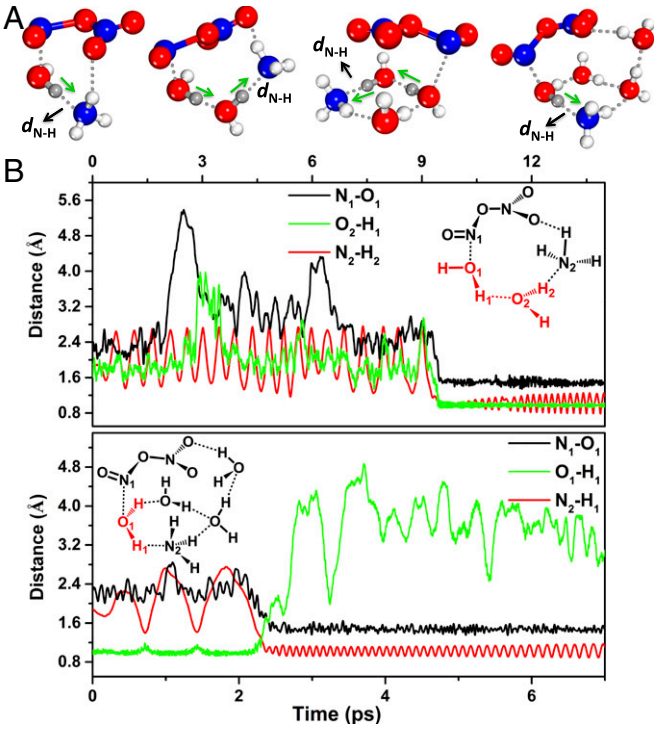

Fig. 1. (*A*) Initial structures of the monohydrate, dihydrate, trihydrate, and tetrahydrate systems used for the metadynamics simulations. The white, blue, and red balls represent the H, N, and O atoms, respectively. The gray balls indicate the H atoms that shift along the direction indicated by the green arrows and bind to the neighboring molecule. (*B*) The *Middle* and *Bottom* panels present the time evolution of the N_1–O_1, N_2–H_2, and O_2–H_1 lengths and the N_1–O_1, O_1–H_1, and N_2–H_1 lengths for the dihydrate and tetrahydrate systems in the course of the metadynamics simulations, respectively. The *Inset* is the schematic illustration of the structure before the formation of HONO. The H_2O molecules directly involved in reactions are highlighted in red. Note that the double bonds in the NO_3 group are represented by single bonds for a better view of the stereochemical configurations.

for the identification of possible reaction paths that were subsequently investigated in detail using both the climbing-image nudged elastic band (CI-NEB) and thermodynamic integration methods.

In Fig. 1 and *SI Appendix*, Fig. S2 (and Movies S1–S4), the simultaneous formation of NH_4^+ and HONO is observed from the metadynamics simulations in all four systems following two different reaction mechanisms. Fig. 1*B* displays the variation in the N_1–O_1, N_2–H_2, and O_2–H_1 bond lengths for the dihydrate system and the N_1–O_1, O_1–H_1, and N_2–H_1 bond lengths for the tetrahydrate system during the metadynamics simulations. The corresponding bond length variations for the monohydrate and trihydrate systems are shown in *SI Appendix*, Fig. S2. In the dihydrate system, the reaction follows a loop-structure mechanism involving two water molecules, as reported in our previous paper (26). In Fig. 1*B*, two H_2O molecules (in red) bridge $ONONO_2$ and NH_3 via the electrostatic interaction of N_1–O_1 and hydrogen bonding of H_1–O_2 and H_2–N_2, forming a loop structure. Initially (<9.47 ps), the N_2–H_2 length (the collective variable) fluctuates between 1.20 and 2.64 Å. At ∼9.47 ps, a hydrogen atom in the H_2O molecule at the NH_3 end shifts toward the NH_3 molecule, and the N_2–H_2 distance decreases to 0.95 Å, suggesting the formation of NH_4^+. Simultaneously, the H_2O close to the NO motif donates the H_1 atom to the oxygen atom in the H_2O at the NH_3 end, which shortens the H_1–O_2 distance to ∼0.96 Å, and a new H_2O molecule is generated. The remaining OH group combines with the NO motif to yield the HONO species, corresponding to shortening of the N_1–O_1

CHEMISTRY

distance from 2.47 to 1.46 Å. This mechanism involves splitting the two H_2O molecules that bridge $ONONO_2$ and NH_3, and is thus denoted the dual-water mechanism. Similar to our previous report (26), the two water molecules (in red) act as a reaction center with the oxygen atom as the proton transporter. The dual-water mechanism is also observed in the trihydrate system. In *SI Appendix*, Fig. S2, *Lower*, the two water molecules (in red) in the reaction center directly participate in the reaction, whereas the third water molecule more likely acts as a "solvent" molecule. The addition of this solvent molecule lowers the barrier from 7.5 to 4.3 kcal/mol (*SI Appendix*, Fig. S1), which will be further confirmed with the CI-NEB.

Unlike the dihydrate and the trihydrate systems, the reaction occurring in the monohydrate and tetrahydrate systems follows a single-water mechanism. In the monohydrate system, a loop structure is formed with a water molecule bridging the $ONONO_2$ and the NH_3. With the approach of NH_3, the H_2O molecule splits into an OH and an H (in gray) that bind with the NO motif in the $ONONO_2$ and the NH_3 molecules, respectively, thus leading to the formation of the HONO species and NO_3^- and NH_4^+ groups (*SI Appendix*, Fig. S2, *Upper*, and Movie S1). Similarly, in the tetrahydrate system, only one water molecule is directly involved in the HONO formation reaction. In Fig. 1*B*, $ONONO_2$ and NH_3 are bridged through one water molecule (in red) with the other three water molecules surrounding them. At ∼1.21 ps, the N_2–H_1 distance decreases to ∼1.00 Å and is accompanied by an increase in the O_1–H_1 distance, which suggests the formation of NH_4^+ and the dissociation of the water molecule. Simultaneously, the N_1–O_1 distance is shortened to ∼1.47 Å, leading to the formation of the HONO species. During the whole process, no bond breaking and formation are observed in the other three surrounding water molecules. In both the monohydrate and the tetrahydrate systems, the water molecule bridging $ONONO_2$ and NH_3 is the only one that dissociates and directly participates in HONO formation. As such, this mechanism is denoted the single-water mechanism. The reaction barriers involved in this process are 5.2 and 1.8 kcal/mol for the monohydrate and tetrahydrate systems (*SI Appendix*, Fig. S1), respectively.

To gain more insight into the two mechanisms illustrated above, we located the transition state (TS) for all four systems, following both the single- and dual-water mechanisms; the energy profiles are presented in Fig. 2. For the monohydrate system, only the single-water mechanism is considered since only one H_2O molecule is involved. Note that the energy of the reactant states (RSs) shown in Fig. 2 are the average binding energies relative to gas-phase H_2O, N_2O_4, and NH_3 molecules, which is calculated as follows:

$$E_{\text{reactant}} = \frac{E_{\text{system}} - (E_{N_2O_4} + n^*\ E_{H_2O} + E_{NH_3})}{m},$$

where n and m represent the number of water molecules and the total number of molecules in the system, respectively. E_{system} is the energy of the monohydrate, dihydrate, trihydrate, or tetrahydrate system. $E_{N_2O_4}$, E_{H_2O}, and E_{NH_3} represent the energies of the N_2O_4, H_2O, and NH_3 molecules, respectively. The average binding energy reflects the variation in the binding strength within the system. The energies of the TS and the product state (PS) are calculated relative to the corresponding RS. All energies presented in Fig. 2 are the calculated electronic energies with a zero-point energy (ZPE) correction at the B3LYP/6-311++G(3df,2p) level.

Clearly, for both mechanisms, the energy barrier decreases with an increasing number of water molecules in the system. Such an effect is particularly significant for the single-water mechanism. In Fig. 2, *Left*, for the monohydrate system, the single-water mechanism is associated with a barrier as high as 14.4 kcal/mol. The addition of one more water molecule reduces the barrier by ∼74% (3.7 kcal/mol for the dihydrate system). The trihydrate and

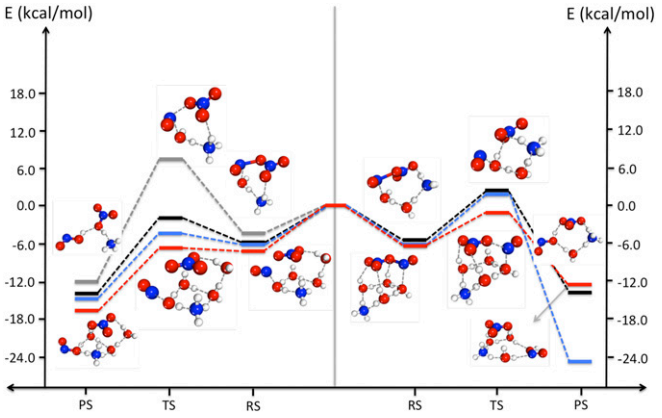

Fig. 2. Energy profiles for HONO in the monohydrates (gray line), dihydrates (black line), trihydrates (blue line), and tetrahydrates (red line) by following the single- (*Left*) and dual-water (*Right*) mechanisms. The same color code that is used in Fig. 1 is used here. More geometric structures of the RS, TS, and PS are shown in *SI Appendix*, Figs. S4 and S5, for the single- and dual-water mechanisms, respectively.

tetrahydrate systems have even lower energy barriers of 1.8 and 0.6 kcal/mol, respectively. The reduction in the barrier with the addition of water molecules is likely due to solvation and stabilization effects of water molecules. A comparison of the RSs in the monohydrate and tetrahydrate systems show that the additional water molecules weaken the π-orbital coupling between the NO motif and the NO_3 groups, as indicated by the highest occupied molecular orbitals in the $ONONO_2$ molecules (*SI Appendix*, Fig. S3). Additional direct evidence is the increase in the bond length between the NO motif and NO_3 group from 1.933 to 2.092 Å and an increased charge separation of the $ONONO_2$ molecule. The charges of the NO_3 group and the NO motif are −0.54/0.45 and −0.63/0.38 $|e|$ for the monohydrates and tetrahydrates (*SI Appendix*, Table S1), respectively, suggesting a larger ionization extension of the $ONONO_2$ molecule, which leads to the formation of a more active NO^+/NO_3^- ion pair. In addition, the net charge of the $ONONO_2$ becomes more negative in the TS (−0.35, −0.38, −0.21, and −0.45 $|e|$ for the monohydrates, dihydrates, trihydrates, and tetrahydrates, respectively), suggesting increased charge transfer between the $ONONO_2$ and $nH_2O + NH_3$ groups. The charged $ONONO_2$ group in the TS can be effectively stabilized by the solvation effect of the $nH_2O + NH_3$ group, a well-established fact in the gas-phase clusters (36–39). The addition of extra water molecules (indicated by green arrows in *SI Appendix*, Fig. S4*A*) around the reaction center enhances such stabilization, leading to a decrease of the energy barrier. *SI Appendix*, Fig. S4*A* clearly shows an enhancement in the hydrogen bonding formed by the surrounding water molecules. For example, in the dihydrate system, the length of the hydrogen bond decreases from 2.019 and 1.866 Å to 1.817 and 1.734 Å in the TS (*SI Appendix*, Fig. S4*A*). In the trihydrate and tetrahydrate systems (*SI Appendix*, Fig. S4 *C* and *B*), the average length of the hydrogen bonds in the TSs is reduced by 0.11 and 0.08 Å compared with that in the corresponding RSs, respectively. As such, the promoted ionization due to the solvation and stabilization effects of the TS cooperatively enhances the reactivity of the $NH_3 + ONONO_2 + nH_2O$ system with increasing n.

In comparison with the single-water mechanism, the dual-water mechanism generally entails higher energy barriers. Additionally, the RSs associated with the dual-water mechanism exhibit a weaker binding strength due to their slightly higher average binding energies than those of their single-water counterparts. In Fig. 2, *Right*, H_2O acts as the proton acceptor in the formation of an H_3O^+ group in the TS, rather than NH_3, as observed in the single-water mechanism. Given the more basic properties of NH_3, it is considered

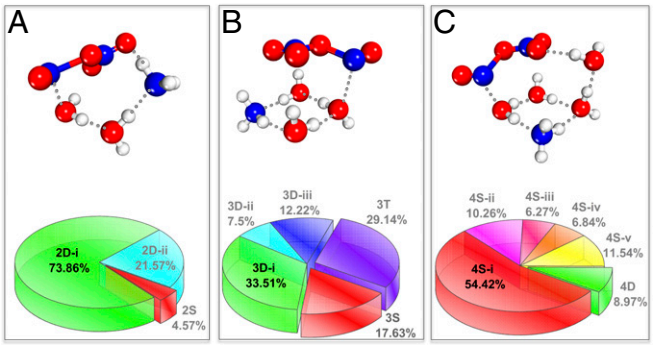

Fig. 3. The *Lower* panels show the populations of different isomers of the (*A*) dihydrate, (*B*) trihydrate, and (*C*) tetrahydrate systems from the corresponding 100-ps BOMD simulations. The *Upper* panels show the most populated structures for each system. The symbols D, S, and T indicate the isomer with dual-, single-, or triple-water molecules, respectively, which bridge the NO motif in the N_2O_4 and NH_3. The geometric structures of the other isomers are presented in *SI Appendix*, Fig. S6.

a better proton acceptor than H_2O. Thus, the dual-water mechanism with H_2O as the first proton acceptor is less favorable than the single-water mechanism where NH_3 acts as the first proton acceptor. However, we previously reported that the dual-water mechanism is very important in the hydrolysis process of SO_3. The difference is due to the different hydrophilic abilities of SO_3 and $ONONO_2$, that is, SO_3 is more hydrophilic than $ONONO_2$ and can bind with H_2O via a stronger S–O interaction. This stronger binding offsets the unfavorable H_2O as the first proton acceptor. Hence, a future study of the dependence of both mechanisms on the hydrophilic ability of various reactant candidates will be insightful.

In addition to the energy barrier, the probability of forming a specific RS structure, which is required for a specific reaction mechanism to occur, is another key factor that affects the activity. The single-water mechanism requires preformation of a structure with one water molecule bridging the NO motif and NH_3 molecule, whereas the dual-water mechanism requires an initial structure where two water molecules act as the bridge connecting the NO motif and the NH_3 molecule. The isomer structure with the former feature is denoted by "S" and the latter by "D." In *SI Appendix*, Fig. S6, the notations 2D-i and 2D-ii represent the isomers of the dihydrate with the D feature but different arrangements of the remaining molecules. A comparison of the ZPE-corrected electronic energies suggests higher stability for the S-featured isomers for all systems considered here. However, the analysis of the snapshot structures from the BOMD simulations shows that the probability distribution of both structures depends on the number of water molecules in the system as shown in Fig. 3. For the dihydrate system, the D-featured isomers exhibit the highest population (74% and 22% for 2D-i and 2D-ii, respectively). Only 5% of the isomers exhibit S features. For the trihydrate system, the most populated isomers still exhibit the D feature with a total population of 53%. However, the population of the S-featured isomer (isomer 3S) increases to 18%, and isomers (3T) with three water molecules bridging the NO motif and NH_3 are present. Notably, the favorability of the population of the S- and D-featured isomers is inverted in the tetrahydrate system, where the S-featured isomer is most populated, and the D-featured isomer has a population percentage of less than 9%. Notably, more than one-half of the isomers exhibit the well-defined structure of the RS that has been proven highly active with low barriers, based upon both metadynamics simulations and reaction path calculations.

Having obtained the most probable structures, we evaluated the relative free-energy variation along the selected reaction coordinates for the monohydrate and tetrahydrate systems using thermodynamic integration. For both systems, the reaction coordinate (also referred to as the collective variable) is chosen as the sum of the N–H and N–O distances. For comparison, we also computed the relative free energy along with the variation in the N–H distance for the dihydrate and pentahydrate systems without the NH_3 molecule. The NH_3-free dihydrate and pentahydrate systems are considered the counterpart of the NH_3-containing monohydrate and tetrahydrate systems, respectively. The free-energy surfaces calculated for all four systems are shown in Fig. 4. The reaction coordinates are normalized with the equation below:

$$R_{\text{normalized}} = \frac{R_{\max} - R_{\text{i}}}{R_{\max} - R_{\min}},$$

where $R_{\max}$, $R_{\min}$, and R_{i} are the maximum, minimum, and instantaneous value of the collective variable at each point. As shown by the gray line in Fig. 4, without the NH_3 molecule, a relatively high free-energy barrier of 8.2 kcal/mol is encountered for the formation of the HONO species, solely from one N_2O_4 and two H_2O molecules, and the reaction is endergonic by 4.3 kcal/mol, suggesting that HONO formation is unfavorable. The addition of three water molecules reduces the free-energy barrier to 5.6 kcal/mol, but the reaction remains endergonic by 1.2 kcal/mol. In contrast to the NH_3-free systems, HONO formation in the NH_3-containing monohydrate and tetrahydrate systems has a lower free-energy barrier, and the reaction is exergonic. Compared with the NH_3-free dihydrate system, the NH_3-containing monohydrate system can be viewed, simply, as replacing one H_2O with one NH_3 molecule. However, the reaction becomes exergonic by 5.8 kcal/mol, and the free-energy barrier is lowered to 5.8 kcal/mol, in contrast to the endergonic and high-barrier reaction associated with the NH_3-free dihydrate system. The addition of three more H_2O molecules to the NH_3-containing monohydrate

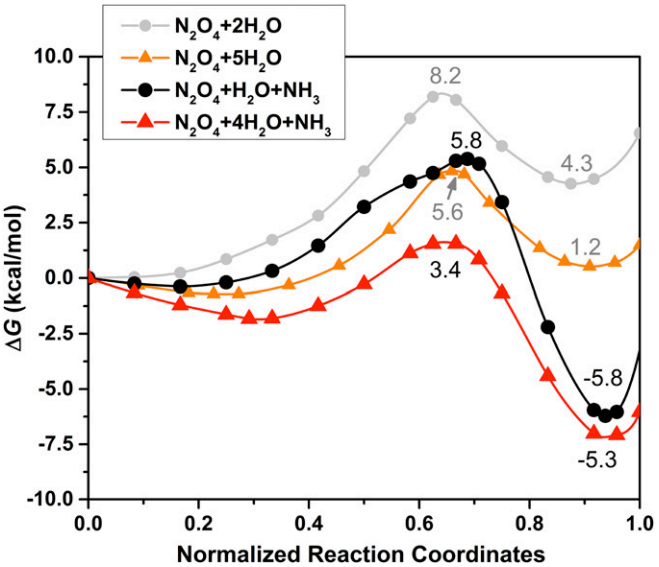

Fig. 4. Relative free-energy variation (ΔG) along the corresponding reaction coordinates obtained from the thermodynamic integration methods. For NH_3-containing ($N_2O_4 + H_2O + NH_3$ and $N_2O_4 + 4H_2O + NH_3$) and NH_3-free ($N_2O_4 + 2H_2O$ and $N_2O_4 + 5H_2O$) systems, the collective variable is scanned every 0.2 Å from 2.4 to 4.8 Å and every 0.1 Å from 1.4 to 2.5 Å, respectively. One or more scanning points are interpolated to locate the minimum or the maximum points. For each single point, the constraint BOMD simulation runs for 5 ps and the next 10- to 15-ps simulation results are used for the free-energy calculation. The free-energy difference is obtained via an integration of the average Lagrange multiplier that is the average force required to constrain the collective variable at the desired value.

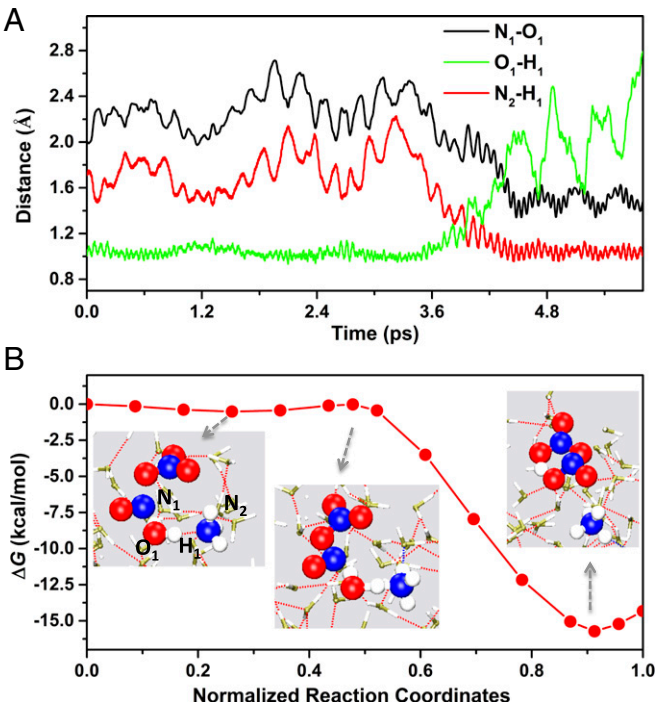

Fig. 5. (*A*) Time evolution of the N_1–O_1, O_1–H_1, and N_2–H_1 lengths during the BOMD simulation of N_2O_4 + NH_3 on the water droplet surface. (*B*) Relative free-energy variation (ΔG) along the corresponding reaction coordinates obtained from thermodynamic integration methods.

system further reduces the free-energy barrier to 3.4 kcal/mol, ~2.2 kcal/mol lower than that of the NH_3-free counterpart (the pentahydrate system). Moreover, the resulting HONO and NH_4NO_3 species are stabilized by 5.3 kcal/mol. Therefore, the more basic NH_3 molecule helps stabilize the hydrated HONO + NO_3 system and reduces the free-energy barrier of the reaction, thereby promoting the formation of HONO.

In addition to clusters in the atmosphere, water can also exist in the liquid phase as water droplets and solvents in, or surrounding, aerosol particles. The water content and the air–water interface in these systems have been shown to have a catalytic role toward various chemical reactions (26, 40–42). Here, we further investigated the reaction of $ONONO_2$ and NH_3 on the surface of a water droplet via both BOMD and thermodynamic integration. The formation of HONO is directly observed in the BOMD simulation via a single-water mechanism (Movie S5) with a free-energy barrier as low as 0.5 kcal/mol. In Fig. 5*A*, before 3.6 ps, the N_1–O_1 and N_2–H_1 distances vary from 1.98 to 2.70 and 1.47–2.20 Å, indicating the relative stability of the N_2O_4 and NH_3 compounds on the droplet surface. The O_1–H_1 distance fluctuates by ~1 Å, suggesting that no water splitting occurs. At 3.6 ps, the elongation of the O_1–H_1 bond length in the water molecule bridging $ONONO_2$ and NH_3 emerges, accompanied by a shortening of the N_1–O_1 and N_2–H_1 bond lengths. Upon summiting a TS, as shown in the second *Inset* images in Fig. 5*B*, the water molecule dissociates into a H atom and a OH group, corresponding to an elongation in the O_2–H_1 bond length from 1.00 to 1.60 Å. Simultaneously, the resulting H atom binds to NH_3, and the OH group binds to the NO motif, leading to the formation of the NH_4^+ ion and the HONO species. During the whole process, bond breaking only occurs on one water molecule, suggesting that the single-water mechanism is the same as that in the tetrahydrate system. Following the single-water mechanism, the free-energy barrier is 0.5 kcal/mol, much lower than in the tetrahydrate system (3.4 kcal/mol). The reaction is also over twice as exergonic (15.3 kcal/mol) than the tetrahydrate system (5.3 kcal/mol). The extremely low barrier and the high exergonic property of the reaction on the water droplet surface result from the existence of a complex hydrogen-bond network. Compared with the RS, the TS and the PS show more ionic properties and can be further stabilized by the complex hydrogen-bond network due to the formation of the solvation shell around ionic chemicals (i.e., NO_3^- and NH_4^+) (36–39). Hence, we have demonstrated that water droplets promote the formation of HONO from the reaction between $ONONO_2$ and NH_3 with a free-energy barrier comparable to k_BT at room temperature.

Conclusions

In conclusion, we have studied the role of gaseous NH_3 molecules in the formation of HONO from N_2O_4 and H_2O using several theoretical methods. Two distinctly different mechanisms, the single- and the dual-water mechanisms, are identified from metadynamics simulations. CI-NEB calculations confirm that the single-water mechanism is generally more favorable than the dual-water mechanism. Solvation effects from additional water molecules in the systems further lower the energy barrier, promoting the formation of HONO. The configuration statistics from the BOMD simulations show that the dihydrate and trihydrate systems preferentially form the RS structure (the structure with the D feature) of the dual-water mechanism, whereas the structure with the S feature required for the single-water mechanism has the highest population in the tetrahydrate system. Overall, the formation of HONO in the monohydrate and tetrahydrate systems tends to follow the single-water mechanism, whereas the dual-water mechanism appears to be more favorable in the dihydrate and trihydrate systems.

More importantly, a comparison of the free energy of HONO formation from the NH_3-free and NH_3-containing hydrated N_2O_4 systems demonstrates the promoting role of NH_3 toward HONO formation. The involvement of NH_3 molecules in the system leads to a stabilization of the PSs, making HONO formation exergonic rather than endergonic, as observed in NH_3-free systems, while notably lowering the free-energy barrier required for HONO formation. The free-energy barrier is as low as 3.4 kcal/mol in the NH_3-containing tetrahydrate system. Moreover, the free-energy barrier can be further reduced to 0.5 kcal/mol when the formation of the HONO species is on the surface of a water droplet, confirming the important role of water droplets in promoting atmospheric chemistry. Hence, the NH_3-promoted HONO formation from hydrated N_2O_4 is an important source of HONO in the atmosphere. In highly polluted areas where NH_3 is relatively abundant, its contribution is even more important, a conclusion consistent with previous field observations.

Methods

The Gaussian and plane-wave (GPW) method implemented in the CP2K Quickstep package (43) is used in the BOMD simulations, metadynamics simulations, and thermodynamic integration methods. The wave functions expanded in a triple-ζ Gaussian basis set with additional auxiliary basis sets are used to treat the valence electrons (44, 45), whereas the Goedecker–Teter–Hutter (GTH) norm-conserved pseudopotentials are adopted to model the core electrons (46). The energy cutoffs for the finest grid level and Gaussian wave are set as 300 and 40 Ry, respectively. The Becke–Lee–Yang–Parr (BLYP) functional method (47, 48) and Grimme's dispersion correction method (49) are employed to describe the electron exchange and correlation and the London dispersion interaction, respectively (denoted the BLYP-D method). For all BOMD simulations (including those involved in the metadynamics simulations and thermodynamic integration methods), the constant-volume and constant-temperature (*NVT*) ensemble is adopted, and the time step is set as 0.5 and 1 fs for the cluster and droplet models, respectively. Temperature is controlled at 300 K using the Nosé–Hoover chain method (50, 51).

A large supercell (20 × 20 × 20 $Å^3$) is chosen to minimize the interaction between two neighboring clusters for the NH_3 + N_2O_4 + nH_2O systems (n = 1, 2, 3, and 4). A (20 × 20 $Å^2$) water slab (as shown in the *Inset* image of *SI*

Appendix, Fig. S7) with a thickness of ∼15 Å is used to simulate the water droplet system. The initial structure is first stabilized with classic force field methods for ∼100 ps and is followed by an ∼20-ps BOMD simulation at 300 K. The tetrahydrate ($NH_3 + N_2O_4 + 4H_2O$) structure from the ∼100-ps MD simulation is placed onto the surface of the prestabilized water slab. The structure is further stabilized with the BOMD simulation for an additional 15 ps by fixing the reaction center (highlighted in the *Inset* images of *SI Appendix*, Fig. S7). The obtained structure is used for further BOMD simulations with all atoms free to move. To narrow the sample space, a quadratic wall is applied with a force constant of 20 kcal/mol when the sum of the N_1–O_1 and N_2–H_1 lengths (as labeled in Fig. 5*B*) is larger than 4.5 Å.

For the reaction path search, we use the CI-NEB method (52), implemented in the TSASE toolkit. The B3LYP functional with the 6-311++G(3df, 2p) basis sets (48, 53) and Grimme's dispersion correction, implemented in the Gaussian 09 package, are used to evaluate the force and energy of each image. The convergence criterion for the force on each image is set to be 0.02 eV/Å. The vibrational frequencies for each TS are computed to confirm that only one imaginary frequency exists. The ZPE correction is included in the energy profile. To validate the parameters used here, we compute the heat of reaction for the reaction $2NO_2 + H_2O \rightarrow HONO + HNO_3$ using both the CP2K and Gaussian 09 packages. The obtained values are −5.75 and −7.32 kcal/mol, which are acceptable compared with the experimental value of -6.7 ± 0.6 kcal/mol (54). We also compute the energy barrier for the reaction $ONONO_2 + H_2O \rightarrow HONO + HNO_3$ with presence of one NH_3 molecule. The obtained energy barriers of 12.26 and 14.35 kcal/mol based on the CP2K and Gaussian 09 packages, respectively, are comparable.

ACKNOWLEDGMENTS. Calculations were done at the University of Nebraska Holland Computing Center, the National Energy Research Scientific Computing Center, and the Texas Advanced Computing Center. This work was supported by National Science Foundation Grant CHE-1665325 and the Welch Foundation (F-1841).

1. Harris GW, et al. (1982) Observations of nitrous acid in the Los Angeles atmosphere and implications for predictions of ozone-precursor relationships. *Environ Sci Technol* 16:414–419.
2. Alicke B, Platt U, Stutz J (2002) Impact of nitrous acid photolysis on the total hydroxyl radical budget during the limitation of oxidant production/Pianura Padana Produzione di Ozono study in Milan. *J Geophys Res* 107:LOP 9-1–LOP 9-17.
3. Kleffmann J, et al. (2005) Daytime formation of nitrous acid: A major source of OH radicals in a forest. *Geophys Res Lett* 32:L05818.
4. An JL, et al. (2013) Enhancements of major aerosol components due to additional HONO sources in the North China Plain and implications for visibility and haze. *Adv Atmos Sci* 30:57–66.
5. Hou SQ, Tong SR, Ge MF, An JL (2016) Comparison of atmospheric nitrous acid during severe haze and clean periods in Beijing, China. *Atmos Environ* 124:199–206.
6. Li G, et al. (2010) Impacts of HONO sources on the photochemistry in Mexico City during the MCMA-2006/MILAGO campaign. *Atmos Chem Phys* 10:6551–6567.
7. Kleffmann J (2007) Daytime sources of nitrous acid (HONO) in the atmospheric boundary layer. *ChemPhysChem* 8:1137–1144.
8. Michoud V, et al. (2014) Study of the unknown HONO daytime source at a European suburban site during the MEGAPOLI summer and winter field campaigns. *Atmos Chem Phys* 14:2805–2822.
9. Spataro F, et al. (2013) Occurrence of atmospheric nitrous acid in the urban area of Beijing (China). *Sci Total Environ* 447:210–224.
10. Huang RJ, et al. (2017) Concentration and sources of atmospheric nitrous acid (HONO) at an urban site in Western China. *Sci Total Environ* 593–594:165–172.
11. Kirchstetter TW, Harley RA, Littlejohn D (1996) Measurement of nitrous acid in motor vehicle exhaust. *Environ Sci Technol* 30:2843–2849.
12. Veres P, et al. (2010) Measurements of gas-phase inorganic and organic acids from biomass fires by negative-ion proton-transfer chemical-ionization mass spectrometry. *J Geophys Res* 115:D23302.
13. Stockwell WR, Calvert JG (1983) The mechanism of NO3 and HONO formation in the nighttime chemistry of the urban atmosphere. *J Geophys Res* 88:6673–6682.
14. Li S, Matthews J, Sinha A (2008) Atmospheric hydroxyl radical production from electronically excited NO_2 and H_2O. *Science* 319:1657–1660.
15. Ammann M, et al. (1998) Heterogeneous production of nitrous acid on soot in polluted air masses. *Nature* 395:157–160.
16. Kleffmann J, Becker KH, Wiesen P (1998) Heterogeneous NO_2 conversion processes on acid surfaces: Possible atmospheric implications. *Atmos Environ* 32:2721–2729.
17. Stemmler K, Ammann M, Donders C, Kleffmann J, George C (2006) Photosensitized reduction of nitrogen dioxide on humic acid as a source of nitrous acid. *Nature* 440:195–198.
18. Scharko NK, Berke AE, Raff JD (2014) Release of nitrous acid and nitrogen dioxide from nitrate photolysis in acidic aqueous solutions. *Environ Sci Technol* 48:11991–12001.
19. Finlayson-Pitts BJ, Wingen LM, Sumner AL, Syomin D, Ramazan KA (2003) The heterogeneous hydrolysis of NO_2 in laboratory systems and in outdoor and indoor atmospheres: An integrated mechanism. *Phys Chem Chem Phys* 5:223–242.
20. Chou A, Li ZR, Tao FM (1999) Density functional studies of the formation of nitrous acid from the reaction of nitrogen dioxide and water vapor. *J Phys Chem A* 103:7848–7855.
21. Luo G, Chen X (2012) Ground-state intermolecular proton transfer of N_2O_4 and H_2O: An important source of atmospheric hydroxyl radical? *J Phys Chem Lett* 3:1147–1153.
22. Liu J, et al. (2015) Mechanism of the gaseous hydrolysis reaction of SO_2: Effects of NH_3 versus H_2O. *J Phys Chem A* 119:102–111.
23. Bandyopadhyay B, Biswas P, Kumar P (2016) Ammonia as an efficient catalyst for decomposition of carbonic acid: A quantum chemical investigation. *Phys Chem Chem Phys* 18:15995–16004.
24. Sarkar S, Mallick S, Deepak, Kumar P, Bandyopadhyay B (2017) Isomerization of methoxy radical in the troposphere: Competition between acidic, neutral and basic catalysts. *Phys Chem Chem Phys* 19:27848–27858.
25. Mallick S, Sarkar S, Bandyopadhyay B, Kumar P (2018) Effect of ammonia and formic acid on the $OH^{\bullet}$ + HCl reaction in the troposphere: Competition between single and double hydrogen atom transfer pathways. *J Phys Chem A* 122:350–363.
26. Li L, et al. (2016) Near-barrierless ammonium bisulfate formation via a loop-structure promoted proton-transfer mechanism on the surface of water. *J Am Chem Soc* 138:1816–1819.
27. Mount GH, et al. (2002) Measurement of atmospheric ammonia at a dairy using differential optical absorption spectroscopy in the mid-ultraviolet. *Atmos Environ* 36:1799–1810.
28. Wilson SM, Serre ML (2007) Examination of atmospheric homes, and schools ammonia levels near hog CAMS, in Eastern North Carolina. *Atmos Environ* 41:4977–4987.
29. Ge C, Zhu C, Francisco JS, Zeng XC, Wang J (2018) A molecular perspective for global modeling of upper atmospheric NH_3 from freezing clouds. *Proc Natl Acad Sci USA* 115:6147–6152.
30. Cheng MT, Chen SP, Lin YC, Jung CC, Horng CL (2008) Concentrations and formation rates of ambient nitrous acid in Taichung City, Taiwan. *Environ Eng Sci* 25:1149–1157.
31. Bari A, Ferraro V, Wilson LR, Luttinger D, Husain L (2003) Measurements of gaseous HONO, HNO_3, SO_2, HCl, NH_3, particulate sulfate and PM2.5 in New York, NY. *Atmos Environ* 37:2825–2835.
32. Wang G, et al. (2016) Persistent sulfate formation from London Fog to Chinese haze. *Proc Natl Acad Sci USA* 113:13630–13635.
33. Wang X, et al. (2016) Theoretical study of the gaseous hydrolysis of NO_2 in the presence of NH_3 as a source of atmospheric HONOI. *Environ Chem* 13:611–622.
34. Seifert NA, et al. (2017) The gas-phase structure of the asymmetric, *trans*-dinitrogen tetroxide (N_2O_4), formed by dimerization of nitrogen dioxide (NO_2), from rotational spectroscopy and *ab initio* quantum chemistry. *J Chem Phys* 146:134305.
35. de Jesus Medeiros D, Pimentel AS (2011) New insights in the atmospheric HONO formation: New pathways for N_2O_4 isomerization and NO_2 dimerization in the presence of water. *J Phys Chem A* 115:6357–6365.
36. Botti A, Bruni F, Imberti S, Ricci MA, Soper AK (2005) Solvation shell of H^+ ions in water. *J Mol Liq* 117:77–79.
37. Miller DJ, Lisy JM (2006) Mimicking solvent shells in the gas phase. II. Solvation of K^+. *J Chem Phys* 124:024319.
38. Raugei S, Klein ML (2001) Dynamics of water molecules in the Br^- solvation shell: An ab initio molecular dynamics study. *J Am Chem Soc* 123:9484–9485.
39. Stace AJ (2002) Metal ion solvation in the gas phase: The quest for higher oxidation states. *J Phys Chem A* 106:7993–8005.
40. Calvert JG, et al. (1985) Chemical mechanisms of acid generation in the troposphere. *Nature* 317:27–35.
41. Clifford D, Donaldson DJ (2007) Direct experimental evidence for a heterogeneous reaction of ozone with bromide at the air-aqueous interface. *J Phys Chem A* 111:9809–9814.
42. Gerber RB, et al. (2015) Computational studies of atmospherically-relevant chemical reactions in water clusters and on liquid water and ice surfaces. *Acc Chem Res* 48:399–406.
43. VandeVondele J, et al. (2005) Quickstep: Fast and accurate density functional calculations using a mixed Gaussian and plane waves approach. *Comput Phys Commun* 167:103–128.
44. VandeVondele J, Hutter J (2007) Gaussian basis sets for accurate calculations on molecular systems in gas and condensed phases. *J Chem Phys* 127:114105.
45. Lippert G, Hutter J, Parrinello M (1997) A hybrid Gaussian and plane wave density functional scheme. *Mol Phys* 92:477–487.
46. Goedecker S, Teter M, Hutter J (1996) Separable dual-space Gaussian pseudopotentials. *Phys Rev B Condens Matter* 54:1703–1710.
47. Becke AD (1988) Density-functional exchange-energy approximation with correct asymptotic behavior. *Phys Rev A Gen Phys* 38:3098–3100.
48. Lee C, Yang W, Parr RG (1988) Development of the Colle-Salvetti correlation-energy formula into a functional of the electron density. *Phys Rev B Condens Matter* 37:785–789.
49. Grimme S, Antony J, Ehrlich S, Krieg H (2010) A consistent and accurate ab initio parametrization of density functional dispersion correction (DFT-D) for the 94 elements H-Pu. *J Chem Phys* 132:154104.
50. Nose S (1984) A unified formulation of the constant temperature molecular-dynamics methods. *J Chem Phys* 81:511–519.
51. Hoover WG (1985) Canonical dynamics: Equilibrium phase-space distributions. *Phys Rev A Gen Phys* 31:1695–1697.
52. Henkelman G, Uberuaga BP, Jonsson H (2000) A climbing image nudged elastic band method for finding saddle points and minimum energy paths. *J Chem Phys* 113:9901–9904.
53. Becke AD (1993) Density-functional thermochemistry. 3. The role of exact exchange. *J Chem Phys* 98:5648–5652.
54. Chase JMW (1998) *NIST-JANAF Thermochemical Tables* (American Institute of Physics, Woodbury, NY), 4th Ed.